Frequency-Domain Time-Resolved Four Wave Mixing Spectroscopy of Vibrational Coherence Transfer with Single-Color Excitation

Andrei V. Pakoulev,* Mark A. Rickard, Nathan A. Mathew, Kathryn M. Kornau, and John C. Wright

Department of Chemistry, University of Wisconsin, Madison, Wisconsin 53706

Received: November 19, 2007; Revised Manuscript Received: February 29, 2008

Triply vibrationally enhanced four-wave mixing spectroscopy is employed to observe vibrational coherence transfer between the asymmetric and symmetric CO-stretching modes of rhodium(I) dicarbonyl acetylacetonate (RDC). Coherence transfer is a nonradiative transition of a coherent superposition of quantum states to a different coherent superposition due to coupling of the vibrational modes through the bath. All three excitation pulses in the experiment are resonant with a single quantum coherence, but coherence transfer results in new coherences with different frequencies. The new output frequency is observed with a monochromator that resolves it from the stronger peak at the original excitation frequency. This technique spectrally resolves pathways that include coherence transfer, discriminates against spectral features created solely by radiative transitions, and temporally resolves modulations created by interference between different coherence transfer pathways. Redfield theory simulates the temporal modulations in the impulsive limit, but it is also clear that coherence transfer violates the secular approximation invoked in most Redfield theories. Instead, it requires non-Markovian and bath memory effects. RDC may provide a simple model for the development of theories that incorporate these effects.

Introduction

Pump−probe spectroscopy is the most common method for measuring ultrafast dynamics in chemical systems.[1–5] A pump pulse excites a population and a probe measures the population's temporal evolution. Coherent multidimensional spectroscopy (CMDS) expands the capabilities of pump−probe spectroscopy by using two excitation pulses for the pump step. Four wave mixing (FWM) CMDS uses three excitation pulses to create an output pulse. The first pulse excites a coherence and the second creates a population. Alternatively, if the second pulse has a different frequency, it can excite a zero- or double-quantum coherence that is analogous to multiquantum coherences in heteronuclear multiple quantum coherence (HMQC) NMR.[6,7] The third pulse converts the population to an output coherence that measures the population dynamics (or alternatively the zero- and double-quantum coherence dynamics). Scanning the second time delay measures the same population dynamics as pump−probe experiments but scanning the first or third time delays measures the dynamics of the first or last coherences. Usually, the coherence dynamics is dominated by dephasing or rephasing processes. However, CMDS also allows direct observation of coherence transfer (CT), a process that is usually not directly observed. CT results when the thermal bath induces the evolution of one of the states involved in a coherence to form a different coherence.[8–11] CT is the analogue of population relaxation at the quantum mechanical amplitude level.

It is now becoming clear that CT can play an important role in ultrafast dynamics because it allows one to observe the quantum-state evolution while the system remains coherent. For example, time domain FWM-CMDS experiments in the Fenna−Matthews−Olson photosynthetic light-harvesting protein show that CT during the primary events of photosynthesis results in the evolution of a zero quantum coherence of two different excitonic states to form zero-quantum coherences with most other excitonic states of the complex.[12] This coherent coupling may be quite important because it may provide an efficient mechanism for coherent energy flow to the reaction center. In vibrational CMDS, CT provides an alternative mechanism to identify which vibrational modes are coupled. Tokmakoff's group first observed peaks in their time domain 2D-IR spectra that were attributed to two coordinated CT events.[13] The peak positions defined the first and last coherences but because the time domain methods excite all quantum states, the transitions connecting the first and last coherences were not experimentally defined.

Mixed frequency/time domain methods such as triply vibrationally enhanced (TRIVE) FWM spectroscopy use pulse widths that are long enough to excite specific transitions but short enough to resolve the ultrafast dynamics.[7,14,15] TRIVE-FWM methods identified single CT processes where the CT shifted the output frequency by the frequency difference between the two states involved in the transfer.[16] The narrow line widths of the excitation pulses define all of the transitions involved in the CT. Typically, CT involves several coherence pathways that are quantum mechanically equivalent and interfere to create characteristic modulations in the output signals. The phase matching conditions for TRIVE-FWM could also be changed to reject the normal FWM processes and isolate the processes involving CT.[17] It is thus becoming clear that CT can play an important role in the developing field of CMDS.

In this article, we describe a new TRIVE-FWM method that uses single color excitation pulses to create output frequencies that are shifted by the frequency difference between states involved in CT. These new frequencies are not present without CT and are signatures of the CT process. Thus, a simple monochromator scan of the output frequencies can identify the presence of CT processes that originate in the initially excited

---

* Corresponding author. E-mail: pakoulev@chem.wisc.edu.

FWM CMDS of Vibrational Coherence Transfer

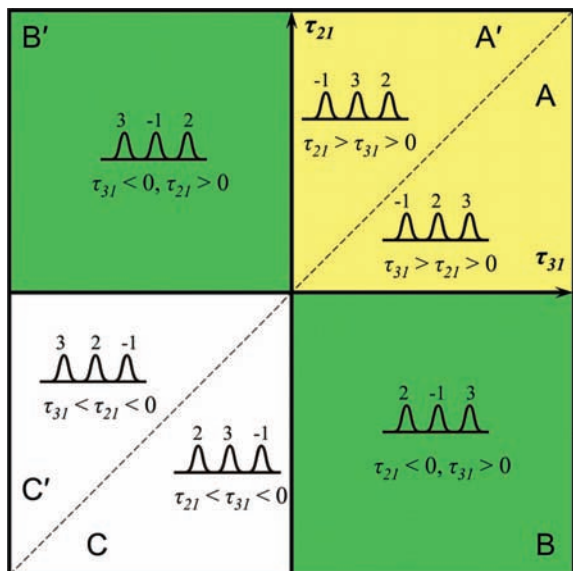*J. Phys. Chem. A, Vol. 112, No. 28, 2008* **6321**

Figure 1. Temporal sequence of excitation pulses in TRIVE experiment with the phase-matching condition $\mathbf{k}_4 = -\mathbf{k}_1 + \mathbf{k}_2 + \mathbf{k}_3$ in the time frame $\tau_{21} = \tau_2 - \tau_1$ vs $\tau_{31} = \tau_3 - \tau_1$. Here, τ_i's refer to actual pulse positions in time; subscripts $i = 1, 2, 3$ refer to different laser pulses. The τ_{21}, τ_{31} space is divided into three regions A, B and C. Pulse sequences labeled as A′, B′ and C′ are equivalent to A, B and C, respectively, because all the laser pulses have the same frequency.

quantum state. These CT processes in turn define the quantum states that are coupled to the initially excited quantum state. This demonstrates that CMDS is possible with a single excitation frequency using pulses that are resonant with a single vibrational or electronic transition and a monochromator that detects output coherences at frequencies that have been shifted by CT. Again, we show that there are multiple coherence pathways that differ in the time ordering of the CT and these interfere to create characteristic modulations in the delay time dependences of the CT signals. The modulations define the relative signs of all the transfer processes. Additional isolation of a CT signal resulting from a single color excitation is also possible through the phase-matching conditions. The length of the nonlinear polarization wave vector for a noncollinear phase-matching geometry is defined by the lengths and directions of the excitation wave vectors. However, CT changes the wave vector of the output electric field because the output frequency changes. Adjusting the directions of the laser beams optimizes the phase matching for the CT peak and suppresses the main peak which is now phase mismatched.

Theoretical Background

The TRIVE method in this work is a coherent FWM process where three laser beams at frequencies ω_1, ω_2, and ω_3 create coherences that generate a fourth coherent beam at the frequency $\omega_4 = -\omega_1 + \omega_2 + \omega_3$. Frequency domain TRIVE involves scanning ω_1, ω_2, and ω_3 while measuring the output intensity. Cross-peaks appear in a multidimensional spectrum from the intramolecular coupling and anharmonicity of the vibrational modes. To increase the spectral selectivity of TRIVE-FWM, the output signal is measured with a monochromator at the frequency $\omega_m = \omega_4$. If all the excitation pulses have the same frequency, ω, the output signal is expected at the same frequency so $\omega_4 = \omega$. On the other hand, CT changes one vibrational coherence (or population) into a different vibrational coherence and therefore creates a new frequency component that is resolved from the main TRIVE signal by the monochromator.
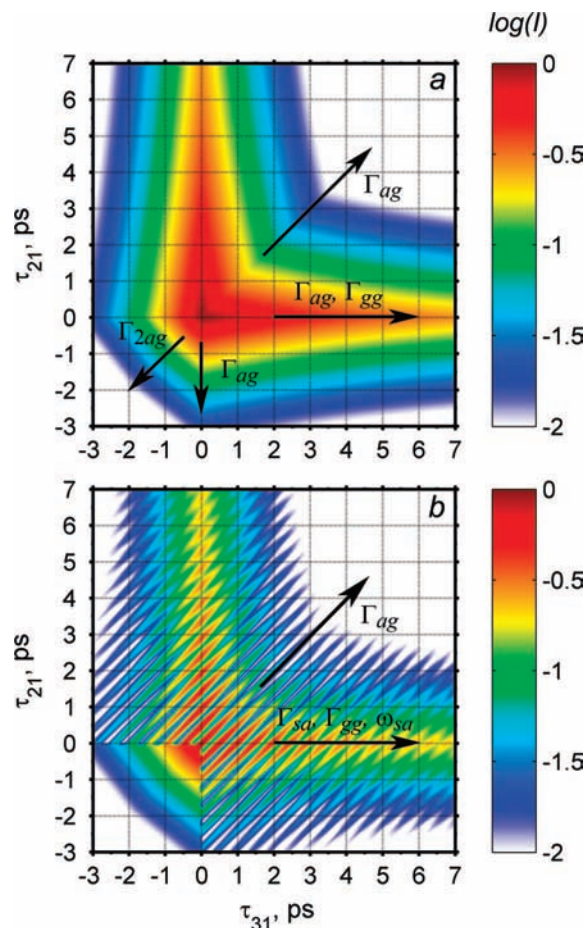

Figure 2. Theoretical simulation of the TRIVE signal intensity in the impulsive limit using the parameters summarized in Table 1 for two cases: (a) $\omega_1 = \omega_2 = \omega_3 = \omega_m = \omega_{ag} = 2015$ cm^{-1} (main TRIVE peak). (b) $\omega_1 = \omega_2 = \omega_3 = 2015$ cm^{-1}, $\omega_m = \omega_{sg} = 2084$ cm^{-1} (CT peak). Also shown is the set of parameters that define the system dynamics if the delay scan is performed along the corresponding arrows (see text for explanation).

Our model of the CT in TRIVE[16,17] is based on the Redfield theory of relaxation processes[9] and the treatment developed by Stenholm for collisional CT[18] and Hayashi et al.[19] for quantum beats in time-resolved coherent anti-Stokes Raman scattering. Redfield theory describes the relaxation dynamics for the population and coherence density matrix elements of a quantum system interacting with a thermal bath. Equation 1 describes the temporal evolution of the $\rho_{mn} = |m\rangle\langle n|$ density matrix elements of the m and n states in the presence of an excitation pulse and relaxation processes.

$$\dot{\rho}_{mn} = \left(-i\omega_{mn} - \sum_{kl \neq mn} \kappa_{kl,mn}\right)\rho_{mn} + \sum_{kl \neq mn} \kappa_{mn,kl}\rho_{kl} + i\sum_i (\Omega_{mi}\rho_{in} - \Omega_{in}\rho_{mi}) \quad (1)$$

Here, ω_{mn} is the oscillation frequency of ρ_{mn}, Ω_{mi} is the Rabi frequency of the $i \rightarrow m$ transition, and $\kappa_{kl,mn}$ is the Redfield tensor element for the transfer rate from ρ_{mn} to ρ_{kl} using conventional tetradic notation.[9] The term $\sum_{kl \neq mn} \kappa_{kl,mn}$ is the dephasing rate Γ_{mn} of ρ_{mn} (or population relaxation rate of ρ_{mm}). The term $\sum_{kl \neq mn} \kappa_{mn,kl}\rho_{kl}$ describes nonradiative feeding of ρ_{mn} from populations, ρ_{kk}, and coherences, ρ_{kl}, and the last terms describe feeding by radiative transitions from ρ_{in} or ρ_{mi} that are induced by the electromagnetic field.

In the impulsive approximation, the radiative feeding term in eq 1 creates the ρ_{mn} coherence. In our model, this coherence now serves as the initial condition, ρ_{mn}^0, for subsequent excitation pulses that probe the relaxation dynamics of the quantum system. Because our excitation pulse bandwidth is sufficiently narrow that only a single vibrational state is excited, coherence transfer cannot occur from other vibrational states. Therefore, we assume that ρ_{mn} is not perturbed by coherence transfer from other states involved in ρ_{kl} with $kl \neq mn$. In addition, we assume that the CT rate from ρ_{mn}^0 is appreciably smaller than the dephasing rate ($\kappa_{kl,mn} \ll \Gamma_{mn} = \sum_{kl \neq mn} \kappa_{kl,mn}$) so we can neglect coherence transfer back from any coherences created by transfer from ρ_{mn}^0 (i.e., neglect double CT, $\rho_{mn}^0 \overset{CT}{\Rightarrow} \rho_{kl} \overset{CT}{\Rightarrow} \rho_{mn}$ relative to $\rho_{mn}^0 \overset{CT}{\Rightarrow} \rho_{kl}$).

With these assumptions, the excitation pulse arriving at time τ instantaneously creates an initial coherence $\rho_{mn}^0(\tau)$, which subsequently undergoes free induction decay:

$$\rho_{mn}(t-\tau) = \theta(t-\tau)\, \rho_{mn}^0(\tau)\, e^{(-i\omega_{mn} - \Gamma_{mn})(t-\tau)} \qquad (2)$$

where $\theta(t)$ is a Heaviside step function and τ refers to the temporal position of the excitation pulse. Inhomogeneous broadening effects are not considered. Because the excitation pulse excites only one vibrational state, the dynamics of the ρ_{kl} coherence created by CT from ρ_{mn}, $\rho_{mn} \overset{CT}{\Rightarrow} \rho_{kl}$, can be described by the equation

$$\dot{\rho}_{kl} = (-i\omega_{kl} - \Gamma_{kl})\rho_{kl} + \kappa_{kl,mn}\rho_{mn} \qquad (3)$$

with the initial conditions $\rho_{kl}^0(\tau) = 0$ and $\rho_{mn}^0(\tau) \neq 0$. The solution is

$$\rho_{kl}(t) = \theta(t-\tau)\, \rho_{mn}^0(\tau)\, \frac{\kappa_{kl,mn}}{i(\omega_{mn} - \omega_{kl}) + \Gamma_{mn} - \Gamma_{kl}} \times$$
$$[e^{(-i\omega_{kl} - \Gamma_{kl})(t-\tau)} - e^{(-i\omega_{mn} - \Gamma_{mn})(t-\tau)}] \qquad (4)$$

If $\kappa_{kl,mn}$ was comparable to $|\omega_{kl} - \omega_{mn}|$, the CT would change the oscillation frequency of the initial and final coherences.[18] We will assume the CT is slow so $\kappa_{kl,mn}$ does not affect the dynamics of the destination coherence but does define its magnitude. In addition, we will assume $\Gamma_{kl}, \Gamma_{mn} \ll |\omega_{kl} - \omega_{mn}|$ so the amplitude of the destination coherence is defined only by the $\kappa_{kl,mn}/|\omega_{kl} - \omega_{mn}|$ ratio.

To find an expression for the output TRIVE signal, we use a perturbative approach[20,21] to define the effects of a series of excitation pulses. The initial amplitude of $\rho_{mn}^0(\tau)$ depends on the integrated Rabi frequency and the amplitude of the previous coherence at the time of the impulsive excitation, τ (either $\rho_{in}(\tau)$ or $\rho_{mi}(\tau)$ in eq 1). Thus, the value of $\rho_{mn}^0(\tau)$ includes the dynamics created by previous excitation pulses. If the previous coherence (ρ_{in}, for example) was created by an impulsive excitation at τ_1, its subsequent evolution will be

$$\rho_{in}(t-\tau_1) = \theta(t-\tau_1)\, \rho_{in}^0(\tau_1)\, e^{(-i\omega_{in} - \Gamma_{in})(t-\tau_1)} \qquad (5)$$

If the next impulsive excitation creates ρ_{mn} at $t = \tau_2$, the temporal evolution of ρ_{mn} will be

$$\rho_{mn} = \theta(t-\tau_2)\, \theta(\tau_2 - \tau_1) \times$$
$$i \cdot \Omega_{mi}\rho_{in}^0(\tau_1)\, e^{(-i\omega_{in} - \Gamma_{in})(\tau_2 - \tau_1)}\, e^{(-i\omega_{mn} - \Gamma_{mn})(t-\tau_2)} \qquad (6)$$

where we applied the initial condition at time τ_2:

$$\rho_{mn}^0(\tau_2) = i \cdot \Omega_{mi}\rho_{in}^0(\tau_1)\, e^{(-i\omega_{in} - \Gamma_{in})(\tau_2 - \tau_1)} \qquad (7)$$

Following the perturbative approach, we must add the amplitudes from all the temporal pathways that contribute to

the TRIVE signal to properly account for the quantum mechanical interference effects. The effects depend on the particular temporal sequence of excitation pulses. Figure 1 shows all possible time orderings for the phase-matching condition $\mathbf{k}_4 = -\mathbf{k}_1 + \mathbf{k}_2 + \mathbf{k}_3$ using the time delays of $\tau_{21} = \tau_2 - \tau_1$ (vertical axis) vs $\tau_{31} = \tau_3 - \tau_1$ (horizontal axis) where τ_i denotes the actual temporal position of the excitation pulse labeled i. Note that the labels do not correspond to the time ordering but are instead defined by the phase matching. Thus, the delay τ_{ij} is positive if the pulse i arrives after the pulse j ($\tau_i > \tau_j$) and negative if the pulse i is ahead of the pulse j ($\tau_i < \tau_j$). The frequencies of all three excitation beams are identical in this experiment. Because the $\mathbf{k}_2$ and $\mathbf{k}_3$ beams act identically with our phase matching condition, the coherence pathways will not change upon permutation of indices 2 and 3 but they will depend upon permutations of index 1 with any other index. Hence, the dependence of the output signal on delays τ_{21} and τ_{31} is expected to be symmetric relative to the diagonal (dashed line in Figure 1). We divided the τ_{21}, τ_{31} space into three regions (the time orderings are designated as A, B and C and are given different colors). Pulse sequences that permute indices 2 and 3 are labeled as A′, B′ and C′ and are equivalent to A, B and C, respectively. We will focus on the case $\tau_{31} > \tau_{21}$.

First, let us consider the main TRIVE peak when all the excitation pulses are resonant with the transition between the ground state (g) and a specific quantum state (a). We assume no coherence transfer occurs and the output signal and excitation frequencies are identical ($|\omega_m| = |\omega_1| = |\omega_2| = |\omega_3| = |\omega_{ag}|$). The important coherence pathways depend on the time ordering of the excitation pulses. The pathways are

Time ordering A ($\tau_{31} > \tau_{21} > 0$):

$$g,g \xrightarrow{-1} g,a \xrightarrow{2} a,a \xrightarrow{3} a,g \qquad (8a)$$

$$g,g \xrightarrow{-1} g,a \xrightarrow{2} g,g \xrightarrow{3} a,g \qquad (8b)$$

Time ordering B ($\tau_{31} > 0$, $\tau_{21} < 0$):

$$g,g \xrightarrow{2} a,g \xrightarrow{-1} a,a \xrightarrow{3} a,g \qquad (9a)$$

$$g,g \xrightarrow{2} a,g \xrightarrow{-1} g,g \xrightarrow{3} a,g \qquad (9b)$$

Time ordering C ($\tau_{21} < \tau_{31} < 0$):

$$g,g \xrightarrow{2} a,g \xrightarrow{3} 2a,g \xrightarrow{-1} a,g \qquad (10)$$

In this notation we use letters to define density matrix elements (populations or coherences), arrows to define the excitation interaction, and numbers to define the excitation pulse. For time orderings A and B the interaction with the first pulse creates a coherence (g,a or a,g), the second pulse establishes population in the excited state (a,a) or bleaching in the ground state (g,g), and the third pulse creates the final coherence that radiates at the frequency ω_{ag}. Pathways that involve overtones, such as $g,g \xrightarrow{-1} g,a \xrightarrow{2} a,a \xrightarrow{3} 2a,a$ and $g,g \xrightarrow{2} a,g \xrightarrow{-1} a,a \xrightarrow{3} 2a,a$, are also possible. They are not considered here because the overtone anharmonicity in the a,a → 2a,a transition[22] shifts the output frequency, $\omega_{2a,a}$, by 11 cm^{-1} so it is not detected

FWM CMDS of Vibrational Coherence Transfer

J. Phys. Chem. A, Vol. 112, No. 28, 2008 **6323**

TABLE 1: Dephasing and Population Relaxation Rates Used for Simulations on Figures 2 and 4

coherences				populations	
$1/\Gamma_{ag}$	$1/\Gamma_{sg}$	$1/\Gamma_{sa}$	$1/\Gamma_{2a,g}$	$1/\Gamma_{gg}$	$1/\Gamma_{aa}$
1.5 ps	2.0 ps	2.5 ps	0.8 ps	60 ps	4 ps

by our monochromator when it is tuned to the ω_{ag} output frequency. On the other hand, we do include time ordering C where the only possible pathway does include the overtone transitions a,g $\rightarrow$ 2a,g and 2a,g $\rightarrow$ a,g as intermediates. The spectral width of the excitation pulses ($\sim$20 cm^{-1}) is sufficient to excite these transitions and the final output coherence occurs at the ω_{ag} frequency of the monochromator. In addition, the overtone 2a,g should have a shorter dephasing time and a broader spectral width that facilitates the transition even when the excitation pulses are somewhat detuned. Finally, in the harmonic approximation, the dipole moment for transitions a,g $\rightarrow$ 2a,g and 2a,g $\rightarrow$ a,g is $\sqrt{2}$ larger than g,g $\rightarrow$ a,g.

In the impulsive limit, the output coherence resulting from the three different time orderings is found by following the strategy outlined by eqs 5–7, where each successive density matrix element in each pathway is related to the previous density matrix element. The process begins with the initial ground-state population, ρ_{gg}^0. When multiple pathways exist, the output coherence requires the summation over each pathway. As an example, the final coherence for the time ordering A can be described by the equation

$$\rho_{ag}(t,\tau_1,\tau_2,\tau_3) = \theta(t-\tau_3)i^3\Omega_{ag}^3\rho_{gg}^0 \times$$

$$[e^{(-i\omega_{ag}-\Gamma_{ag})(\tau_2-\tau_1)}e^{-\Gamma_{aa}(\tau_3-\tau_2)}e^{(-i\omega_{ag}-\Gamma_{ag})(t-\tau_3)} +$$

$$e^{(-i\omega_{ag}-\Gamma_{ag})(\tau_2-\tau_1)}e^{-\Gamma_{gg}(\tau_3-\tau_2)}e^{(-i\omega_{ag}-\Gamma_{ag})(t-\tau_3)}] \quad (11)$$

where the first and second terms describe pathways (8a) and (8b), respectively. The frequency distribution of the output intensity requires the Fourier transformation $\rho_{ag}(t) \rightarrow \rho_{ag}(\omega)$ to define the signal measured by the monochromator at $\omega = \omega_{ag}$. The output intensity I is then proportional to $\rho(\omega_{ag})\cdot\rho^*(\omega_{ag})$.

Following this procedure for the time orderings A, B, and C (i.e., eqs 8a,b, 9a,b and 10), the dependence of the TRIVE signal on time delays is

$$I_A(\tau_{31},\tau_{21}) \propto \frac{1}{\Gamma_{ag}^2}(e^{-\Gamma_{aa}|\tau_{31}-\tau_{21}|}+e^{-\Gamma_{gg}|\tau_{31}-\tau_{21}|})^2 e^{-2\Gamma_{ag}|\tau_{21}|}$$

$$(12)$$

$$I_B(\tau_{31},\tau_{21}) \propto \frac{1}{\Gamma_{ag}^2}(e^{-\Gamma_{aa}|\tau_{31}|}+e^{-\Gamma_{gg}|\tau_{31}|})^2 e^{-2\Gamma_{ag}|\tau_{21}|} \quad (13)$$
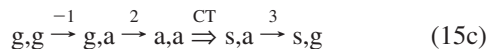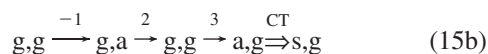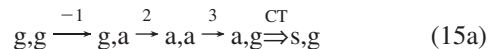
$$I_C(\tau_{31},\tau_{21}) \propto \frac{2}{\Gamma_{ag}^2} e^{-2\Gamma_{ag}|\tau_{31}-\tau_{21}|} e^{-2\Gamma_{2ag}|\tau_{31}|} \quad (14)$$

Expressions for time orderings A′, B′ and C′ result from permutation of indices 2 and 3. Figure 2 a shows the simulation of all the time ordered pathways. Note that it clearly shows the permutation symmetry. The parameters used in the simulations are summarized in Table 1. The τ_{31} and τ_{21} time delays use absolute values to keep an explicit negative sign in the exponential arguments. At $\tau_{21} = 0$ eqs 12 and 13 have the same behavior, so pathways A and B become identical along the X-axis of Figure 2a. Time delay scans of the signal along the τ_{31}-axis (see the horizontal arrow in Figure 2a) have a multiexponential dependence on τ_{31} and the Γ_{aa} and Γ_{gg} population relaxation rates. For the time orderings A and A′,
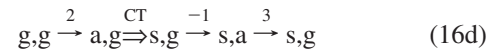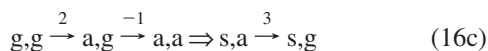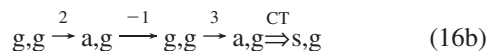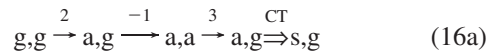
the diagonal scan with a fixed $\tau_{31} - \tau_{21}$ has a dephasing rate $2\Gamma_{ag}$. Pathways B and C become equivalent at $\tau_{31} = 0$, and a delay scan along this axis (vertical arrow on Figure 2a) also exhibits the dephasing rate $2\Gamma_{a,g}$, whereas the decay rate for a diagonal scan in time ordering C exhibits the dephasing rate of the overtone $2\Gamma_{2a,g}$.

Just as normal TRIVE output signal depends on the interference between equivalent pathways, there are equivalent pathways involving CT. This paper describes work where either an excitation of the antisymmetric stretch, labeled "a", undergoes CT to the symmetric stretch mode, labeled "s", or vice versa. The CT pathways include either intermediate coherences or populations, and interference between them must be included in a quantitative description. The pathways involving a single CT may be derived from the fundamental TRIVE pathways (8)−(10) by allowing the CT event to occur after each interaction with an excitation pulse. The successive excitation transitions are limited to those that are resonant with an a $\leftrightarrow$ g transition and lead to the formation of the new s,g output coherence. An analysis shows that the phase-matching conditions do not involve bra-side CT (for example, g,g $\xrightarrow{-1}$ g,a $\xrightarrow{CT}$ g,s $\xrightarrow{2}$ a,s $\xrightarrow{3}$ 2a,s) because it leads to formation of the 2a,s output coherence. A radiative 2a,s $\rightarrow$ s,s transition is forbidden in the harmonic approximation because it requires a three quantum vibrational transition that destroys two quanta in state a and creates one quantum in state s. In time ordering C we also exclude CT pathway g,g $\xrightarrow{2}$ a,g $\xrightarrow{3}$ 2a,g $\xrightarrow{CT}$ (a + s),g $\xrightarrow{-1}$ s,g because this pathway involves a combination band with $\sim$21 cm^{-1} anharmonic shift, so that (a + s),g $\rightarrow$ s,g transition is not sufficiently resonant with the excitation pulse. These approximations significantly simplify the simulation model and lead to the following pathways:
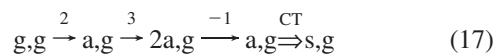
Time ordering A ($\tau_{21} > \tau_{31} > 0$):

$$g,g \xrightarrow{-1} g,a \xrightarrow{2} a,a \xrightarrow{3} a,g \xRightarrow{CT} s,g \quad (15a)$$

$$g,g \xrightarrow{-1} g,a \xrightarrow{2} g,g \xrightarrow{3} a,g \xRightarrow{CT} s,g \quad (15b)$$

$$g,g \xrightarrow{-1} g,a \xrightarrow{2} a,a \xRightarrow{CT} s,a \xrightarrow{3} s,g \quad (15c)$$

Time ordering B ($\tau_{21} > 0$, $\tau_{31} < 0$):

$$g,g \xrightarrow{2} a,g \xrightarrow{-1} a,a \xrightarrow{3} a,g \xRightarrow{CT} s,g \quad (16a)$$

$$g,g \xrightarrow{2} a,g \xrightarrow{-1} g,g \xrightarrow{3} a,g \xRightarrow{CT} s,g \quad (16b)$$

$$g,g \xrightarrow{2} a,g \xrightarrow{-1} a,a \xRightarrow{CT} s,a \xrightarrow{3} s,g \quad (16c)$$

$$g,g \xrightarrow{2} a,g \xRightarrow{CT} s,g \xrightarrow{-1} s,a \xrightarrow{3} s,g \quad (16d)$$

Time ordering C ($\tau_{31} < \tau_{21} < 0$):

$$g,g \xrightarrow{2} a,g \xrightarrow{3} 2a,g \xrightarrow{-1} a,g \xRightarrow{CT} s,g \quad (17)$$

Time orderings A and B have multiple pathways to the output coherence and interfere to create the observed temporal dependence. Figure 3 shows a more detailed summary of these pathways along with energy-level diagrams.
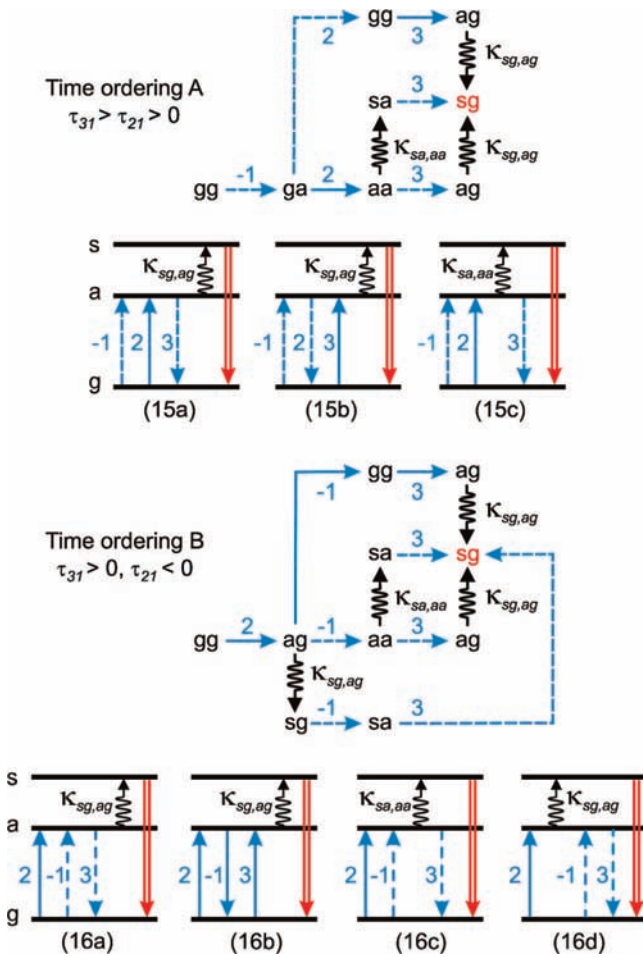
Figure 3. Liouville and energy level diagrams showing coherence flow from initial ground-state population g,g to the final radiating coherence s,g (red) showing all possible pathways with a single CT event for the time orderings A and B (eqs 15 and 16). All laser pulses are resonant with a ↔ g transitions; numbers represent different laser pulses. Solid blue arrows refer to ket-side radiative transitions, dashed blue arrows refer to bra-side radiative transitions, whereas black waved arrows refer to nonradiative coherence transfer with corresponding Redfield tensor element $\kappa_{sg,ag}$ or $\kappa_{sa,aa}$. Final radiative transition is indicated with double red arrow.

The dynamics resulting from pathways (15)−(17) are simulated by using eq 2 to define the coherence before transfer (ρ_{mn}) and eq 4 to define the coherence after coherence transfer (ρ_{kl}). Equation 4 shows that any coherence created by CT oscillates at two frequencies, the frequency of the original coherence ω_{mn} and the frequency of the destination coherence ω_{kl}. (Note, in our particular case, mn refers to ag or aa, and kl refers to sg or sa). Interference between the positive $e^{(-i\omega_{kl}-\Gamma_{kl})t}$ term and the negative $e^{(-i\omega_{mn}-\Gamma_{mn})t}$ term leads to beats at $\omega_{mn} - \omega_{kl}$ in the output signal as a function of the time delays if the coherence transfer occurs after either the first or the second excitation pulses. However, if CT occurs after the last excitation pulse (pathways 15a,b, 16a,b, and 17), the monochromator selects only the frequency of the destination coherence (ω_{sg}) and the frequency of initial coherence (ω_{ag}) does not contribute to the signal. These ideas then allow one to express the output polarization for the different time orderings as the sum of all possible pathways leading to the output coherence at ω_{sg}. For example, time ordering A is described by the equation

$$P_A^{CT}(t,\tau_{31},\tau_{23}) \propto \frac{\theta(t)i^2\Omega_{ab}{}^3 e^{(-i\omega_{sg}-\Gamma_{sg})t} e^{(-i\omega_{ag}-\Gamma_{ag})|\tau_{21}|}}{\omega_{sa}} \times$$

$$[\kappa_{sa,aa}e^{-\Gamma_{aa}|\tau_{31}-\tau_{21}|} - \kappa_{sg,ag}e^{-\Gamma_{aa}|\tau_{31}-\tau_{21}|} - $$

$$\kappa_{sg,ag}e^{-\Gamma_{gg}|\tau_{31}-\tau_{21}|} - \kappa_{sa,aa}e^{(-i\omega_{sa}-\Gamma_{sa})|\tau_{31}-\tau_{21}|}] \quad (18)$$

Here, the first and last terms in the square brackets result from pathway (15c) and the second and third terms correspond to pathways (15b) and (15a), respectively. Further simplification is possible with the assumption $\kappa_{sa,aa} = \kappa_{sg,ag}$ because the first two terms in square brackets then cancel. This approximation should be valid given that the energy difference is the same for the quantum states in the sa,aa and sg,ag pairs. This simplification leads to the next equation for the output intensity:

$$I_A^{CT}(\tau_{21},\tau_{31}) \propto \frac{\kappa_{sg,ag}{}^2}{\omega_{sa}{}^2\Gamma_{sg}{}^2} e^{-2\Gamma_{ag}|\tau_{21}|}[e^{-2\Gamma_{gg}|\tau_{31}-\tau_{21}|} + e^{-2\Gamma_{sa}|\tau_{31}-\tau_{21}|} + $$

$$2e^{-(\Gamma_{sa}+\Gamma_{gg})|\tau_{31}-\tau_{21}|} \cdot \cos(\omega_{sa}(\tau_{31}-\tau_{21}))] \quad (19)$$

Using the same approach for the other time orderings B and C, one finds similar temporal behaviors:

$$I_B^{CT}(\tau_{21},\tau_{31}) \propto \frac{\kappa_{sg,ag}{}^2}{\omega_{sa}{}^2\Gamma_{sg}{}^2}[e^{-2\Gamma_{gg}|\tau_{31}|} e^{-2\Gamma_{ag}|\tau_{21}|} + $$

$$e^{-2\Gamma_{sa}|\tau_{31}|} e^{-2\Gamma_{sg}|\tau_{21}|} + $$

$$2e^{-(\Gamma_{sa}+\Gamma_{gg})|\tau_{31}|} e^{-(\Gamma_{ag}+\Gamma_{sg})|\tau_{21}|} \cdot \cos(\omega_{sa}(\tau_{31}-\tau_{21}))] \quad (20)$$

$$I_C^{CT}(\tau_{21},\tau_{31}) \propto \frac{2\kappa_{sg,ag}{}^2}{\omega_{sa}{}^2\Gamma_{sg}{}^2} e^{-2\Gamma_{ag}|\tau_{31}-\tau_{21}|} e^{-2\Gamma_{2ag}|\tau_{21}|} \quad (21)$$

The simulation using eqs 19–21 in τ_{31}, τ_{21} space results in the predicted dependence shown in Figure 2b. The parameter values are defined in Table 1.

Equation 19 for the time ordering A predicts that when the delay scan is performed parallel to the diagonal of Figure 1 (i.e., $\tau_{31} - \tau_{21}$ is constant), the signal decays exponentially at the rate $2\Gamma_{ag}$ (shown by diagonal arrow on Figure 2b). However, if one of the delays is fixed (e.g., τ_{21}) whereas the other (τ_{31}) is scanned (horizontal arrow on Figure 2b), the signal will oscillate at the difference frequency $\omega_{sa} = |\omega_{sg} - \omega_{ag}|$. The terms in square brackets in eq 19 also depend on Γ_{sa} and Γ_{gg}. Here, Γ_{sa} is the dephasing rate of the zero-quantum coherence |s⟩⟨a|, and Γ_{gg} is the recovery rate for the population in the ground state. The population recovery should be much longer than any dephasing rate. Thus, at long delays where $\tau_{31} \sim 1/\Gamma_{gg}$, only the first term in eq 19 survives and the oscillations will dampen at the faster rate $\Gamma_{sa} + \Gamma_{gg}$. The simulation of the dependence $I_A^{CT}(\tau_{31})$ with $\tau_{21} = 0.5$ ps, $1/\Gamma_{sa} = 2.5$ ps, and $1/\Gamma_{gg} = 60$ ps is shown on Figure 4. The simulation demonstrates that quantum beats appear only on the short time scale $\tau_{31} \sim 1/\Gamma_{sa}$. The shape of the signal at long delay is defined only by an exponential decay with the longer rate, $1/2\Gamma_{gg} = 30$ ps.

Equation 20 for time ordering B is more complicated than eq 19, but the output signal has similar behavior. A time delay scan of τ_{31} and τ_{21} with fixed $\tau_{31} - \tau_{21}$ shows a multiexponential decay with a composite dependence on Γ_{sg}, Γ_{ag}, Γ_{sa} and Γ_{gg}. If delay τ_{21} is fixed while τ_{31} is scanned, quantum beats appear at the difference frequency ω_{sa}. The normalized dependence of $I_B^{CT}(\tau_{31})$ with fixed $\tau_{21} = 0$ (not shown) has the same shape as the $I_A^{CT}(\tau_{31})$ represented in Figure 4.

Time ordering C has only one pathway because CT takes place at the last step. It does not oscillate at the difference
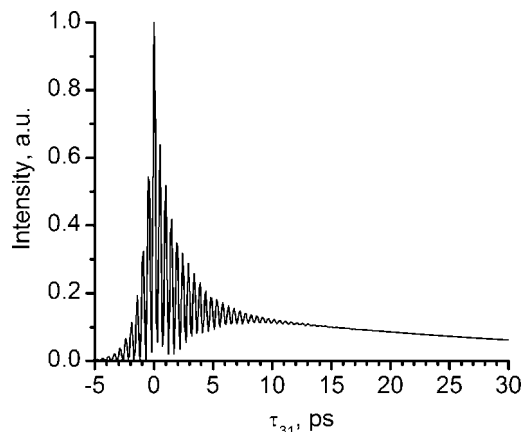
FWM CMDS of Vibrational Coherence Transfer

J. Phys. Chem. A, Vol. 112, No. 28, 2008 **6325**

Figure 4. One-dimensional slice of the simulations shown on Figure 2b at the fixed delay $\tau_{21} = 0.5$ ps. The range of τ_{31} is expanded up to 30 ps to show oscillation damping. If $\tau_{31} > 10$ ps $\gg 1/\Gamma_{ab}$, the kinetics of the signal is defined only by an exponential decay with the rate $1/2\Gamma_{gg} = 30$ ps.

frequency and has the same dependence on delays as the main TRIVE peak (compare eqs 14 and 21).

Experimental Section

The TRIVE experiment was described previously.[7,14,15,17,23] Briefly, it uses a mode-locked Ti:sapphire oscillator/regenerative amplifier to pump two optical parametric amplifiers (OPA). Difference frequency generation creates two tunable pulses in the mid-IR region. The pulse duration is ~900 fs, the spectral width is ~23 cm^{-1}, and the repetition rate is 1 kHz. It is important in these studies that the excitation pulse spectral width be narrow enough that one does not excite both the resonant and nonresonant state. The frequency difference between the two vibrational modes is 69 cm^{-1}. We measured the line shape of the excitation pulse; it closely approximates a Gaussian shape with a fwhm of ~23 cm^{-1}. A Gaussian shape with this width has an expected intensity ~10^{-11} lower than the maximum intensity for the 69 cm^{-1} detuning between the a and s states, ω_{sa}. It was not possible to measure the excitation intensity at this detuning, but it was less than 10^{-6}. The measurement was limited by the scattered light in the monochromator. It is clear that there is negligible excitation of the second vibrational transition when the pulse is resonant with the first vibrational transition.

The output from one OPA is split to form the third excitation beam. All three pulses have the same polarization. Their energies are controlled by apertures and do not exceed 1 μJ. After undergoing adjustable time delays, the three beams are focused into the sample with an off-axis parabolic mirror in a noncollinear phase matching geometry. The TRIVE signal is observed through a monochromator with a liquid nitrogen cooled HgCdTe$_2$ detector. After amplification, the output was digitized with a 12-bit data acquisition card and averaged over 1000–10000 pulses. To minimize pulse-to-pulse fluctuations, the signal was normalized by measuring the energy of each excitation pulse with pyroelectric detectors. This acquisition system allows us to reach a dynamic range up to 10^5. We are also able to change the amplification level of the signal to increase the dynamic range discretely by an additional 2 orders of magnitude, limited only by the electronic noise.

The sample is a 200 μm thick solution of 1.5 mM rhodium(I) dicarbonyl acetylacetonate (Rh(CO)$_2$acac) in hexane contained in a cell with 2 mm thick CaF$_2$ windows. The FTIR spectrum
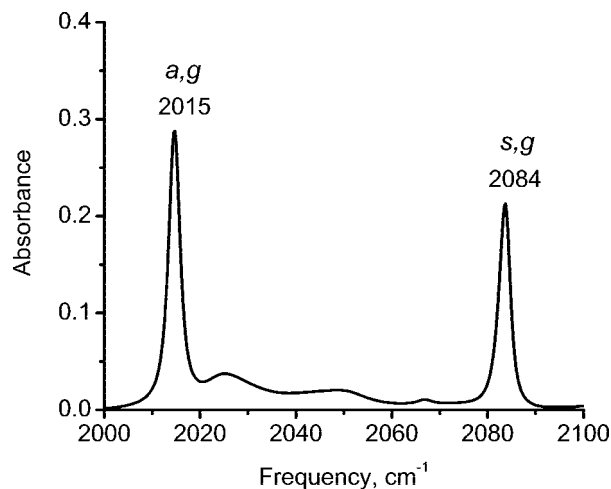

Figure 5. Fourier transform infrared spectrum of the sample. The two peaks are assigned to symmetric (2084 cm^{-1}) and antisymmetric (2015 cm^{-1}) CO stretch mode of rhodium(I) dicarbonyl acetylacetonate.

$$\mathbf{k}_4 = -\mathbf{k}_1 + \mathbf{k}_2 + \mathbf{k}_3$$

$$\mathbf{k}_4' = -\mathbf{k}_1' + \mathbf{k}_2 + \mathbf{k}_3$$

$$|\mathbf{k}_1| = |\mathbf{k}_1'| = |\mathbf{k}_2| = |\mathbf{k}_3| = |\mathbf{k}_4|$$

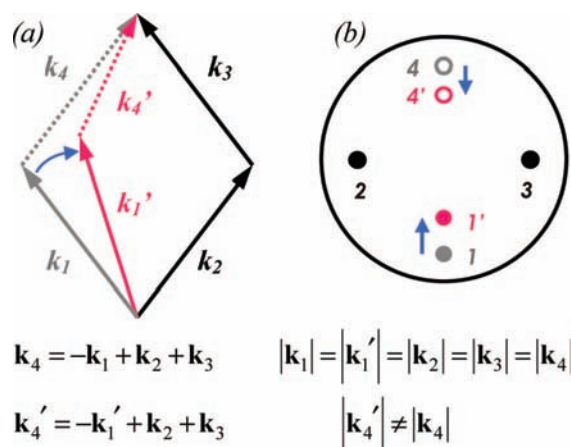$$|\mathbf{k}_4'| \neq |\mathbf{k}_4|$$

Figure 6. Optimization of the phase-matching conditions in TRIVE experiment: (a) simplified wave-vector diagram; (b) projection of the excitation and output beams on the aperture of an off-axis 90° parabolic mirror. The optimal position for the main TRIVE peak is shown in gray. Adjustment to CT geometry (red) requires change in the direction of $\mathbf{k}_1$ to $\mathbf{k}_1'$ and pointing of the output signal from $\mathbf{k}_4$ to $\mathbf{k}_4'$.

of the sample is shown on Figure 5. In this study we excite either the asymmetric (2015 cm^{-1}) or the symmetric (2084 cm^{-1}) CO stretch mode. As described above, the spectral width of the excitation pulses is narrow enough that only one vibrational mode is excited. When the central frequency is resonant with one transition ($\omega_1 = \omega_2 = \omega_3 = 2015$ or 2084 cm^{-1}), the monochromator is tuned to the other vibrational mode ($\omega_m = 2084$ or 2015 cm^{-1}, respectively). The output intensity is recorded as a function of time delays τ_{31} and τ_{21}. Experiments were also performed by scanning the monochromator position at fixed delay times.

Figure 6 illustrates the optimization of the excitation pulse wave vectors for the correct phase-matching conditions for CT. The excitation wave vectors have the same length defined by the frequency of the laser radiation: $|\mathbf{k}_1| = |\mathbf{k}_2| = |\mathbf{k}_3| = n\omega/2\pi c$. Phase matching occurs when the nonlinear polarization's wave vector $-\mathbf{k}_1 + \mathbf{k}_2 + \mathbf{k}_3$ matches the output field's wave vector, $\mathbf{k}_4$. In the first step, the monochromator is tuned to the main TRIVE peak ($\omega_1 = \omega_2 = \omega_3 = \omega_m = \omega$), and the system is aligned to maximize the signal in the direction $\mathbf{k}_4$, where $\mathbf{k}_4 = n\omega/2\pi c$. In the second step, the monochromator is tuned to CT peak at $\omega_m = \omega' \neq \omega$, where the output field's wave vector is $|\mathbf{k}_4'| = n\omega'/2\pi c \neq |\mathbf{k}_4|$. In the third step, the $\mathbf{k}_1$ beam direction
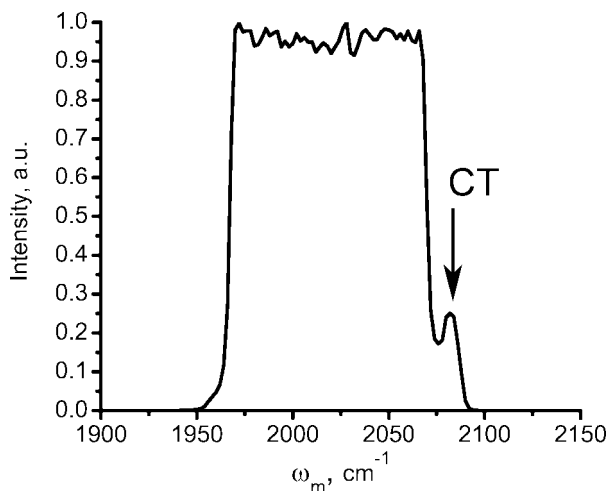
Figure 7. Output spectrum of the TRIVE signal. All laser pulses have the same central frequency $\omega_1 = \omega_2 = \omega_3 = \omega_{ag} = 2015$ cm^{-1}, while ω_m is scanned. The delays between pulses were set as $\tau_{21} = 0.5$ ps and $\tau_{31} = 1$ ps. The main peak at 2015 cm^{-1} is off-scale so one can see the weaker feature at 2084 cm^{-1} (indicated with arrow) from the CTs a,g $\Rightarrow$ s,g and/or a,a $\Rightarrow$ s,a.

Figure 8. Contour plot of log(intensity) versus delays τ_{21} and τ_{31} obtained experimentally for the main TRIVE peak at $\omega_1 = \omega_2 = \omega_3 = \omega_m = 2015$ cm^{-1}.

is changed to $\mathbf{k}_1'$ so that $\mathbf{k}_4' = -\mathbf{k}_1' + \mathbf{k}_2 + \mathbf{k}_3 \neq \mathbf{k}_4$. The main peak is now suppressed because it has a phase mismatch, $|\Delta\mathbf{k}| = n|\omega - \omega'|/2\pi c$. Because $\mathbf{k}_4'$ has not only a different length but also different direction, the alignment of the output beam with the monochromator also requires adjustment. In the actual experiment the excitation beams are focused into the sample cell by an off-axis 90° parabolic mirror. The output is recollimated with another parabolic mirror. The excitation beams' position on the focusing mirror defines the phase matching. Figure 6b shows the projection of the beams on the input aperture and the movements required for optimizing the phase matching. Translating beam 1 to position 1' changes the direction of this beam in the sample and the position of the output beam from 4 to 4' on the recollimating mirror. This approach simplifies the alignment because it allows a continuous adjustment of the phase matching by a single translation stage and results in translation of the output beam along the length of the monochromator slit. Optimizing the phase-matching increases the intensity of the CT peak by more than an order of magnitude.

Results

Figure 7 shows the output spectrum of the TRIVE signal when all excitation pulses are resonant with the transition to the asymmetric (a) CO stretch vibrational mode from the ground state (g), while ω_m is scanned. The delay times were $\tau_{21} = 0.5$ ps and $\tau_{31} = 1$ ps ($\tau_{32} = 0.5$ ps). Because the three laser pulses have the same central frequencies, 2015 cm^{-1}, the peak of the output appears at $\omega_{ag} = 2015$ cm^{-1} and it saturates the detector. The weaker peak appears at $\omega_{sg} = 2084$ cm^{-1} and corresponds to the s,g coherence of the symmetric (s) CO stretch vibration. We attribute this peak to CT, such as a,g $\overset{CT}{\Rightarrow}$ s,g or a,a $\overset{CT}{\Rightarrow}$ s,a. The data in Figure 7 demonstrate not only the presence of CT but also the possibility of CT to higher energy states. CT occurs because of coupling between the vibrational coherences and the bath. The vibrational states' 69 cm^{-1} separation is less than the bath's energy at room temperature ($\sim$200 cm^{-1}) so the bath contributes the energy necessary for CT. However, the intensity of the other CT peak ($\omega_{pump} = 2084$ cm^{-1}, $\omega_m = 2015$ cm^{-1}) was at least double that required by detailed balance.

Figure 8 shows the two-dimensional display of the main TRIVE peak intensity as a function of the τ_{21} and τ_{31} time
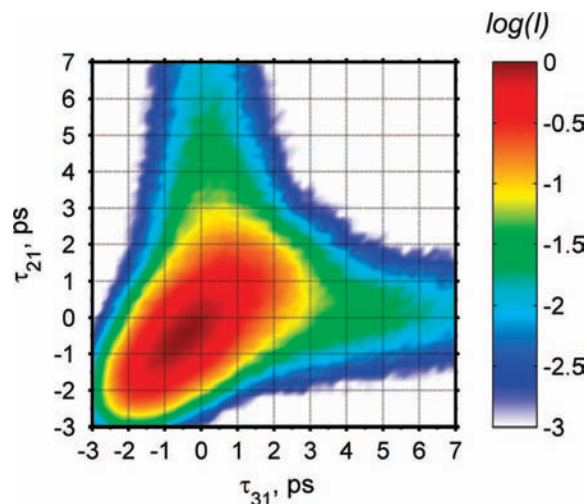
delays. The excitation and monochromator frequencies were tuned to the asymmetric CO stretch transition at $\omega_{ag} = 2015$ cm^{-1}. As previously discussed, the dependence is symmetric about the diagonal. In time orderings A ($\tau_{31} > \tau_{21} > 0$) and B ($\tau_{31} > 0$, $\tau_{21} < 0$), a contour line $I(\tau_{31})$ at fixed τ_{21} exhibits multiexponential decay $I(\tau_{32}) \propto (e^{-\Gamma_{aa}\tau_{32}} + e^{-\Gamma_{gg}\tau_{32}})^2$ with $\Gamma_{aa} = 4$ ps and $\Gamma_{gg} = 60$ ps, which is in good agreement with eq 12 and 13. In time ordering C, the signal is enhanced relative to the simulation in Figure 2a. The enhancement may be related to nonresonant and higher order processes.[24] Note that Figure 8 does not exhibit any temporal modulations that would be present if the CT were rapid enough to perturb the main output coherence.[18] This observation confirms our assumption of slow CT compared with the dephasing rate.

Figure 9 shows the delay scans for two CT peaks. In Figure 9a the excitation frequency is $\omega_{ag} = 2015$ cm^{-1}, while the monochromator is at $\omega_{sg} = 2084$ cm^{-1}. The reverse situation is shown on Figure 9b, where the excitation frequency is $\omega_{sg} = 2084$ cm^{-1}, while the monochromator is at $\omega_{ag} = 2015$ cm^{-1}. In both cases the temporal dependence is similar. The intensity is strongly modulated when one of the delays is fixed while the other is changing. When $\tau_{31} - \tau_{21}$ is constant (cross-sections parallel to diagonal in the space of Figure 9), the signal has a smooth contour with negligible modulations which may be attributed to the small difference in the CT rate constants $\kappa_{sg, ag}$ and $\kappa_{sa, aa}$. The maximum is shifted toward positive delays, so the contribution from time ordering C is small. A cross-section along one of the axes (when one of delays is fixed) shows strong modulations with high contrast at shorter delays. The contrast ratio decreases at longer delays. Contrary to the model shown on Figure 2b, the modulations still exist in region C (see Figure 9a) because the finite pulse duration allows contributions from all time orderings (including A and B) in the region where the excitation pulses overlap, and these contributions interfere to create the modulations.

Figure 10a displays the signal behavior at longer τ_{31} delay times with τ_{21} fixed at 0.5 ps to avoid temporal overlap between time orderings A and B. Figure 10b shows the Fourier transform of Figure 10a. At negative delays (pathway B') and positive delays (pathway A) up to 5 ps the signal is strongly modulated at a frequency of 69 cm^{-1} in Figure 10b, the frequency difference between the vibrational states. At longer delays, the modulation vanishes, and the signal is defined by population dynamics. In contrast to the simulation in Figure 4, this part of
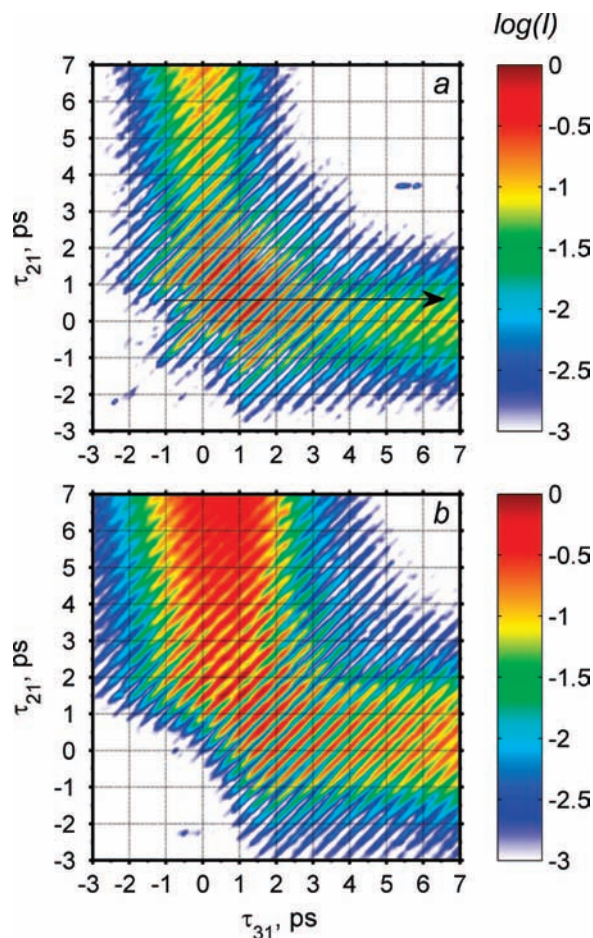
FWM CMDS of Vibrational Coherence Transfer

J. Phys. Chem. A, Vol. 112, No. 28, 2008 **6327**

Figure 9. Contour plot of log(intensity) versus delays τ_{21} and τ_{31} obtained experimentally for the two peaks associated with CT: (a) $\omega_1 = \omega_2 = \omega_3 = \omega_{ag} = 2015$ cm^{-1}, $\omega_m = 2084$ cm^{-1}; (b) $\omega_1 = \omega_2 = \omega_3 = \omega_{sg} = 2084$ cm^{-1}, $\omega_m = 2015$ cm^{-1}. An arrow indicates a trace of one-dimensional scan shown in Figure 10.
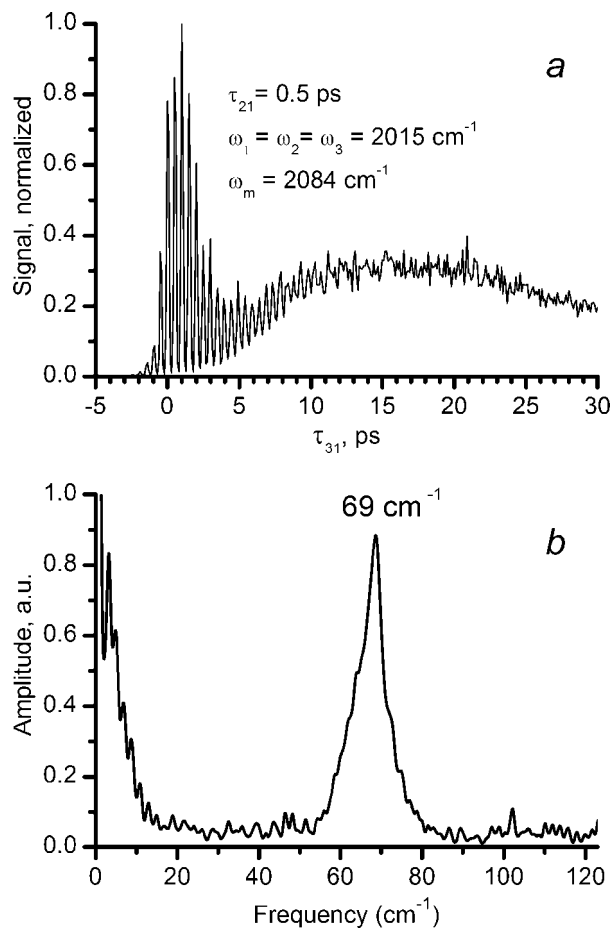

Figure 10. (a) One-dimensional scan of the delay τ_{31} with fixed $\tau_{31} = 0.5$ ps for the CT peak shown on Figure 9a. The scan corresponds to cross-section along arrow on Figure 9a. (b) Direct Fourier transform of data from Figure 10a. Peak at 69 cm^{-1} matches the difference $\omega_{sg} - \omega_{ag} = (2084-2015)$ cm^{-1}.

the kinetic curve rises. Our analysis of additional pathways shows that population exchange followed by CT cannot account for the rise. If, after the second excitation, the population created in one state (for example, a,a) is transferred to the other one (s,s), bra-side CT is needed to create the destination (a,s) coherence. This process has an opposite sign compared to ket-side CT and would interfere destructively with the other pathways. Destructive contribution leads to an additional signal decrease and thus could not explain the rise. We believe the rise is caused by rotational diffusion of excited molecules which occurs on a time scale of several picoseconds.[25]

Discussion

Our previous publications on CT[16,17] focused on the cross-peak created by excitation of two coupled vibrational modes with the laser pulses at two different frequencies. With the proper choice of the phase-matching geometry[17] we were able to suppress coherent multidimensional spectral features created solely by excitation transitions relative to peaks created by CT. However, two-color excitation leads to a large number of CT pathways, while one-color excitation reduces the number of CT pathways to three (for the pulse sequence A) or four (pulse sequence B) and simplifies the analysis of the experimental results. One-color excitation can be performed with a single excitation source, so the experimental system can be simplified as well. In addition, if all optical pulses are resonant with the

same transition, the existence of the output signal at the frequency of a different, spectrally separated transition is direct evidence of CT.

The intensity of the CT signal created in these experiments is $\sim 10^{-4}$–10^{-5} of the main diagonal peak. There are at least two reasons for this low intensity. First, the pre-exponential terms in eqs 12 and 19 show that the ratio of the CT peak to the main peak is $\sim \kappa_{sg,ag}^2/\omega_{sa}^2$ (we assume $\Gamma_{ag} = \Gamma_{sg}$ and $\Omega_{ag} = \Omega_{sg}$ for simplicity). If the CT rate is as large as the dephasing rate of a,g coherence ($\Gamma_{ag} \approx 2$ cm^{-1}), then $\kappa_{sg,ag}^2/\omega_{sa}^2 \sim 10^{-3}$ for $\omega_{sa} = 69$ cm^{-1}. Second, CT changes the symmetry of the third-order susceptibility tensor $\chi_{\alpha\beta\gamma\delta}^{(3)}$ (where indexes refer to Cartesian coordinates). In the case of strong coupling, the two vibrational modes have perpendicular dipole moments, so a $\chi_{xxxx}^{(3)}$ component would transform to $\chi_{xxxy}^{(3)}$. In our experiment, all excitation pulses are vertically polarized. There is no polarization selection at the output except the polarization selectivity of the monochromator grating caused by the vertical orientation of its grooves. CT changes the output polarization, and the grating polarization may cause additional discrimination against the CT peak. Due to rotational diffusion of the excited molecules, the induced polarization anisotropy of the output signal may create an isotropic output, giving the increased output intensity seen in Figure 10a. However, the polarization properties of the CT signal have not yet been studied.

The modulations observed for CT are different from the quantum beating observed in ultrafast experiments or those

related to the interference between zero quantum coherences and populations observed in coherent multidimensional spectroscopy. Quantum beating occurs when either broad-bandwidth excitation pulses excite two separate quantum states[26] or narrow-bandwidth pulses simultaneously excite unresolved quantum states.[27] Zero quantum coherences occur when two excitation pulses create entanglements between two excited quantum states. The CT modulations observed in this study are different, because the energy separation between the two vibrational states (69 cm^{-1}) is much larger than their spectral width (<2 cm^{-1}), and the spectral width of the excitation pulses is too narrow to be resonant with both vibrational transitions.

The modulations caused by CT occur because the destination coherence oscillates at two frequencies (see eq 4): its own frequency (e.g., 2084 cm^{-1}) and the frequency of the coherence that feeds it (2015 cm^{-1}) so the modulation occurs at the difference frequency (69 cm^{-1}). The CT processes observed in this work are not predicted by the secular approximation,[8,28] which is commonly used in the models of intramolecular energy relaxation. This approximation neglects all Redfield tensor terms that do not meet the condition $\omega_{mn} - \omega_{kl} \approx 0$. In the secular approximation the Redfield equations for populations and coherences are decoupled, so that only the population transfer and coherence dephasing terms survive.[26] The observation of the CT modulations in these experiments requires coherent coupling of the significantly different quantum states through the bath. The CT modulations are fingerprints of the coherent relaxation dynamics and they define the modes that are coupled.

In our model of CT we use the impulsive approximation, which neglects the system dynamics during the excitation. Extension of the theory to finite pulse duration requires additional assumptions. The Redfield approach uses the Markovian approximation, which is valid at the time scale $t > \tau_b$, where τ_b is the bath relaxation time.[29] Transient memory effects at the shorter time scale are not included in the Redfield equations. The quantum states and the bath cannot be separated over the time scale of these experiments as the Markovian limit assumes. It has been shown recently that non-Markovian effects can be incorporated into the system dynamics in the second order of perturbation theory,[29] but application of this approach to our experimental situation needs additional development.

The mechanism for CT in these metal chelate molecules is likely related to that observed in a recent heterodyned photon echo study of the Fenna−Matthews−Olson (FMO) bacterio-chlorophyll complex.[12] This study observed modulations of electronic coherences in a photosynthetic system from zero quantum coherences. The study used the same phase matching geometry as our experiment and a pulse sequence that corresponded to pathway A in Figure 1. The modulation depended on the temporal delay between the second and third excitation pulses. The modulation resulted from quantum beating between zero quantum coherences involving all of the excitons in the photosynthetic complex. The different zero quantum coherences were created by the same CT that is normally neglected in most studies of system dynamics. The modulations persisted for a much longer time than expected if population relaxation destroys the coherences. The rapid CT and the long-lived coherences that result both point to the need to incorporate non-Markovian processes and coherent coupling between the system and the thermal bath.

Relaxation between high frequency vibrational modes requires cubic, quartic, or higher order anharmonic terms in the mode coordinates of the interaction Hamiltonian.[11] The cubic term, for example, describes the annihilation of a vibrational quantum

in an initial state, the creation of a vibrational quantum in the new state and the thermal bath[30] or other internal molecular modes. Quartic interactions include creation of two new vibrational states and a quantum state in the bath.[31] The CT processes observed in this work could be created by any of these anharmonicities. For example, the cubic anharmonicity would require bath modes with the 69 cm^{-1} energy difference between the a and s modes. This frequency lies within the range of bath modes that are populated at room temperature (<200 cm^{-1}) so CT transitions involving absorption or emission of bath mode quanta are possible. This type of population dynamics has been reported recently[32] where excitation of OH stretching vibrations in different alcohols resulted in vibrational energy moving through intervening CH_2 or CH groups by emission and absorption of bath quanta until reaching the terminal CH_3 groups. The CT pathways observed in this study include both emission and absorption of bath mode vibrations.

Conclusion

Coherence transfer plays an important role in understanding coherent multidimensional spectra. It has been observed in several different contexts, and it may form the basis for identifying coupling between quantum states. Frequency domain coherent multidimensional spectroscopy provides a way to isolate coherence pathways and coherences that are associated with CT. Frequency domain experiments use narrow bandwidth excitation pulses that define each of the states and coherences that are excited by each of the excitation pulses. In this experiment, three excitation pulses excite a single transition, but CT creates an output that involves different states that are coherently created from the excited coherences. Because there are multiple pathways that are quantum mechanically equivalent, modulations appear when the time delays are changed because of the constructive and destructive interferences between pathways. The experimental results were modeled in the impulsive limit where one neglects the dynamics occurring during the excitation. It will be important to extend the modeling to finite width pulses. This extension will require the inclusion of non-Markovian and bath memory effects because CT becomes insignificant in the secular approximation where these effects are neglected.[8,28] The ability of the mixed frequency/time domain methods to probe CT suggests it is possible to explore the relationship between CT rates and the population and dephasing rates that are known from pump−probe, transient grating, and photon echo experiments.

References and Notes

(1) Jonas, D. M. *Annu. Rev. Phys. Chem.* **2003**, *54*, 425.
(2) Wright, J. C. *Int. Rev. Phys. Chem.* **2002**, *21*, 185.
(3) Wright, J. C.; Zhao, W.; Murdoch, K. M.; Besemann, D. M.; Condon, N. J.; Meyer, K. A. Nonlinear 2D Vibrational Spectroscopy In *Handbook of Vibrational Spectroscopy*; Chambers, J. M., Griffiths, P. R., Eds.; John Wiley and Sons: New York, 2001.
(4) Mukamel, S. *Annu. Rev. Phys. Chem.* **2000**, *51*, 691.
(5) Cho, M. Two Dimensional Vibrational Spectroscopy. In *Advances in Mult-Photon Processes and Spectroscopy*; 1st ed.; Lin, S. H., Villaeys, A. A., Fujimura, Y., Eds.; World Scientific: Singapore, 1999; Vol. 12, p 1.
(6) Mandal, P. K.; Majumdar, A. *Concepts Magn. Reson. Pt. A* **2004**, *20A*, 1.

FWM CMDS of Vibrational Coherence Transfer

J. Phys. Chem. A, Vol. 112, No. 28, 2008 **6329**

(7) Pakoulev, A. V.; Rickard, M. A.; Meyer, K. A.; Kornau, K.; Mathew, N. A.; Thompson, D. C.; Wright, J. C. *J. Phys. Chem. A* **2006**, *110*, 3352.

(8) Uzer, T.; Miller, W. H. *Phys. Rep.—Rev. Sect. Phys. Lett.* **1991**, *199*, 73.

(9) Redfield, A. G. *Adv. Magn. Reson.* **1965**, *1*, 1.

(10) Okazaki, S. Dynamical approach to vibrational relaxation. *Adv. Chem. Phys.* **2001**, *118*, 191.

(11) Kenkre, V. M.; Tokmakoff, A.; Fayer, M. D. *J. Chem. Phys.* **1994**, *101*, 10618.

(12) Engel, G. S.; Calhoun, T. R.; Read, E. L.; Ahn, T.-K.; Mancal, T.; Cheng, Y.-C.; Blankenship, R. E.; Fleming, G. R. *Nature* **2007**, *446*, 782.

(13) Khalil, M.; Demirdoven, N.; Tokmakoff, A. *J. Chem. Phys.* **2004**, *121*, 362.

(14) Besemann, D. M.; Meyer, K. A.; Wright, J. C. *J. Phys. Chem. B* **2004**, *108*, 10493.

(15) Meyer, K. A.; Thompson, D. E.; Wright, J. C. *J. Phys. Chem. B* **2004**, *108*, 11485.

(16) Rickard, M. A.; Pakoulev, A. V.; Kornau, K.; Mathew, N. A.; Wright, J. C. *J. Phys. Chem. A* **2006**, *110*, 11384.

(17) Rickard, M. A.; Pakoulev, A. V.; Mathew, N. A.; Kornau, K. M.; Wright, J. C. *J. Phys. Chem. A* **2007**, *111*, 1163.

(18) Stenholm, S. *J. Phys. B—At. Mol. Opt. Phys.* **1977**, *10*, 761.

(19) Hayashi, M.; Nomura, Y.; Fujimura, Y. *J. Chem. Phys.* **1988**, *89*, 34.

(20) Mukamel, S. *Phys. Rev. A* **1983**, *28*, 3480.

(21) Mukamel, S. *Principles of Nonlinear Optical Spectrscopy*, 1st ed.; Oxford University Press: New York, 1995.

(22) Khalil, M.; Demirdoven, N.; Tokmakoff, A. *J. Phys. Chem. A* **2003**, *107*, 5258.

(23) Meyer, K. A.; Wright, J. C. *Chem. Phys. Lett.* **2003**, *381*, 642.

(24) Mancal, T.; Pisliakov, A. V.; Fleming, G. R. *J. Chem. Phys.* **2006**, *124*, 234504.

(25) Hochstrasser, R. M. *Chem. Phys.* **2001**, *266*, 273.

(26) Pisliakov, A. V.; Mancal, T.; Fleming, G. R. *J. Chem. Phys.* **2006**, *124*, 234505.

(27) Pakoulev, A. V.; Rickard, M. A.; Mathew, N. A.; Kornau, K. M.; Wright, J. C. *J. Phys. Chem. A* **2007**, *111*, 6999.

(28) Tameshtit, A.; Sipe, J. E. *Phys. Rev. A* **1994**, *49*, 89.

(29) Cheng, Y. C.; Silbey, R. J. *J. Phys. Chem. B* **2005**, *109*, 21399.

(30) Deak, J. C.; Iwaki, L. K.; Dlott, D. D. *J. Phys. Chem. A* **1998**, *102*, 8193.

(31) Dlott, D. D. *Chem. Phys.* **2001**, *266*, 149.

(32) Wang, Z. H.; Pakoulev, A.; Dlott, D. D. *Science* **2002**, *296*, 2201.